energies

MDPI

Article

Silicium-Carbide-Based Isolated DC/DC Converter for Medium-Voltage Photovoltaic Power Plants

Minh Nhut Ngo [1,2,*], Philippe Ladoux [2], Jérémy Martin [1] and Sébastien Sanchez [2,3]

[1] Laboratory of Intelligent Management of Electrical Network (LIRE), Department of Solar Technologies (DTS), LITEN, CEA Grenoble, 73370 Le Bourget du Lac, France; jeremy.martin@cea.fr
[2] Laboratory of Plasma and Energy Conversion (LAPLACE), University of Toulouse, 31000 Toulouse, France; philippe.ladoux@laplace.univ-tlse.fr (P.L.); sanchez@laplace.univ-tlse.fr (S.S.)
[3] ICAM, Toulouse Site, 31300 Toulouse, France
* Correspondence: minh-nhut.ngo@cea.fr

Abstract: The production of large-scale photovoltaics (PVs) is becoming increasingly popular in the field of power generation; they require the construction of power plants of several hundred megawatts. Nevertheless, the construction of these PV power plants with conventional low-voltage (LV) conversion systems is not an appropriate technological path. Particularly, large cross-section cables, a high quantity of semiconductors, and the bulky layout of 50/60-Hz step-up transformers make the PV system less competitive in terms of energy efficiency and cost. To overcome these drawbacks, this paper introduces new PV plant topologies with an intermediate medium-voltage direct current (MVDC) collector that requires galvanic isolation for connecting the PV arrays. Then, the design of a power electronic transformer (PET) is proposed, implementing 1.7-kV and 3.3-kV silicium carbide (SiC) power modules. The study confirms that this converter allows the use of medium-frequency (MF) transformers with high power densities while maintaining high efficiency, which facilitates the implementation of isolated medium-voltage (MV) topologies for utility-scale PV power plants.

Keywords: SiC power modules; solid-state transformer; medium-voltage photovoltaic power plant

Citation: Ngo, M.N.; Ladoux, P.; Martin, J.; Sanchez, S. Silicium-Carbide-Based Isolated DC/DC Converter for Medium-Voltage Photovoltaic Power Plants. *Energies* **2022**, *15*, 1038. https://doi.org/10.3390/en15031038

Academic Editor: Alon Kuperman

Received: 22 December 2021
Accepted: 27 January 2022
Published: 29 January 2022

1. Introduction

With the rapid depletion of traditional fossils and other natural resources, nations worldwide are turning to sustainable energy sources that generate carbon-free power. Renewable energy (e.g., solar and wind energy) is considered to be a potential alternative to electricity production by conventional methods. In recent years, investments made for photovoltaic (PV) energy generation have risen significantly [1,2]. Therefore, the construction of PV power plants of several hundred megawatts is under consideration [3]. However, the conventional low-voltage (LV) conversion systems, in which the voltage level is 1500 V for PV strings on the direct-current (DC) side and 690 V/800 V on the alternating-current (AC) side, are no longer being adapted to these power levels. In particular, high-power levels imply high currents and increase the cable cross-sections and number of semiconductors. In addition, the number of 50/60-Hz step-up transformers used to connect the LV power plants to medium-voltage AC (MVAC) grids will increase. This increase will make the PV system less competitive in terms of energy efficiency and cost [4,5]. To overcome these problems, an innovation is to shift toward medium-voltage (MV) levels on both the DC and AC sides [6,7]. Longer PV strings are used with the injection of power to the distribution grid without 50/60-Hz step-up transformers. Recently, scientific articles have reported on the PV technologies and suggested how the transition to MV PV plants could be accepted from a normative point of view [8]. The scope of this paper includes the power electronics part of these new generation power plants.

Now that silicium carbide (SiC) chips are available in the market, found packaged in 1.7 kV and 3.3 kV power modules, it is possible to realize a power electronic transformer (PET) [9,10]. This facilitates the implementation of isolated MV topologies for large-scale PV power plants without using bulky 50/60-Hz transformers. Based on this perspective, the outline of this paper is as follows. Section 2 gives an overview of the possible isolated MV topologies for PV power plants. Section 3 is devoted to the topologies of isolated DC/DC converters. The main conclusions of this research are stated in Section 4.

2. State-of-the-Art Isolated MV Topologies for PV Power Plants

In recent years, several topologies have been proposed. In general, as shown in Figure 1, multiple MVAC collectors are being used, in which three separate cascaded H-bridge inverters connect the PV power plant to the MVAC grid. Galvanic isolation between the PV arrays and the inverter inputs is achieved by isolated DC/DC converters. As shown in Figure 1a, researchers [11–13] have presented a topology in which the input of each isolated DC/DC converter is associated with a PV array. In contrast, a second approach, suggested by [14] and illustrated by Figure 1b, connects a single PV array to a group of converters.

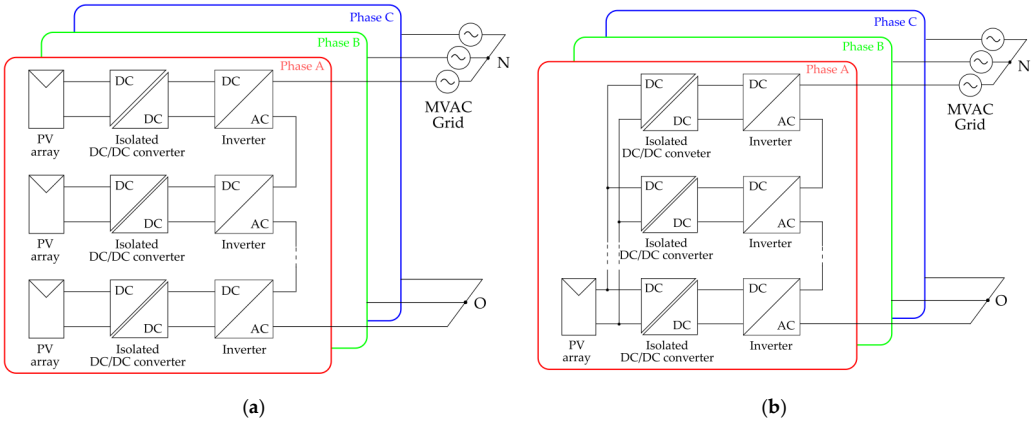

Figure 1. Isolated topologies with multiple MVAC collectors: (**a**) one converter per PV array; (**b**) one group of converters per PV array.

These topologies induce a current imbalance between phases of the MVAC grid. To reduce its affects, control laws proposed by [11–13] can be implemented. Nevertheless, the duty cycle of semiconductors is limited; therefore, the control operating area may be narrow. In other words, power converters risk being oversized when achieving their full capability. Using additional storage devices, such as batteries, also help compensate for the current imbalance [15]. However, this evidently increases the mass of the PV system. Moreover, the single-phase converters require a large filtering of fluctuating power at the input. This fluctuating power also reduces the output power of PV arrays [16]. In the literature, researchers [17–19] have introduced a topology using a multi-winding transformer in order to resolve the current imbalance issue. Nonetheless, this topology is not feasible at high voltage and high-power levels since there are numerous dielectric constraints imposed on the multi-winding transformer.

To naturally cancel the current imbalance, this paper proposes two new topologies in which the connection of the PV power plants to the MVAC grid is performed by a centralized three-phase multilevel inverter. As shown in Figure 2, an intermediate medium-voltage DC (MVDC) collector is established by the series connection of isolated DC/DC converters. The nominal power of the plant can be extended by the parallel association of many groups. In practice, depending on the location of the PV plant, the MVAC grid will have different voltage levels. Thus, the topology of the centralized inverter must also have high modularity, and a modular multilevel converter (MMC) [20,21] will probably be most suitable. This topology is now industrially developed for medium-

voltage applications, such as motor drives, static synchronous compensators (STATCOM), or frequency changers [22–24].

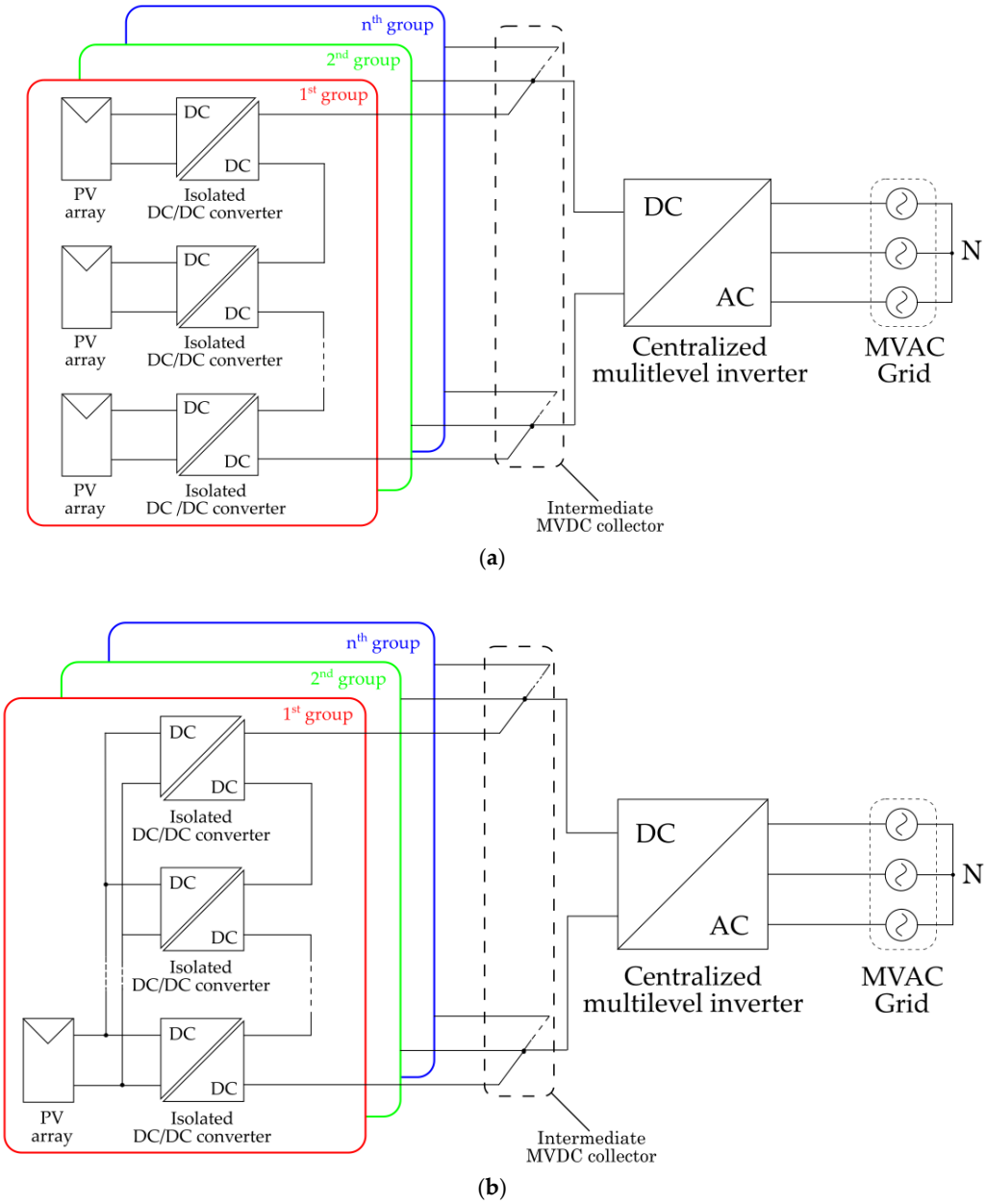

Figure 2. Isolated topologies with an intermediate MVDC collector: (**a**) one converter per PV array; (**b**) one group of converters per PV array.

In Figure 2a, the outputs of the isolated DC/DC converters are connected in series. Therefore, these converters share the same current at their outputs. Power imbalance (due to shading) between PV arrays will affect the voltage sharing in a group. Thus, any converter that provides the lowest level of power will operate with a voltage lower than the nominal voltage. On the other hand, any converter that provides the highest level of power will operate with a voltage higher than the nominal voltage. This can be an issue for the reliability of the semiconductor devices, and then the mean time to failure (MTTF) of the converters. In Figure 1b, one group of converters is associated to a single PV array. Isolated DC/DC converters are associated in input-parallel output-series (IPOS) configuration, which guarantees natural voltage and current balance. Therefore, this topology is more

suitable regarding the converter reliability. In the following sections, the paper will focus on studying the elementary isolated DC/DC converter of the topology presented in Figure 2b.

3. SiC-Based Isolated DC/DC Converter for MV PV Power Plants

As described in Section 2, an isolated step-up topology, based on the association of elementary converters, is required to connect the PV arrays to the intermediate MVDC collector. Hence, in this section, possible topologies for the elementary isolated DC/DC converter are analyzed. For high-power applications, the isolated dual active bridge (DAB) converter is most promising because it allows adaptation to every voltage level [25,26]. It was introduced for the first time in a thyristor-based converter and is currently known as PET [27,28]. The converter consists of an inverter cascaded to an active rectifier via a transformer. With a resonant circuit (e.g., series, parallel, or series–parallel), the DAB converter enables its semiconductors to naturally perform soft-switching operations, that is, zero-voltage switching (ZVS) or zero-current switching (ZCS); this significantly reduces switching losses [29]. The static and dynamic characteristics of semiconductors operating in ZVS and ZCS mode are shown in Figure 3. Consequently, MV power modules can operate at much higher switching frequencies than in the hard-switching mode [30]. Isolated DC/DC converters with high efficiency and power density can be achieved in combination with the outstanding properties of SiC devices and medium-frequency (MF) transformers [26].

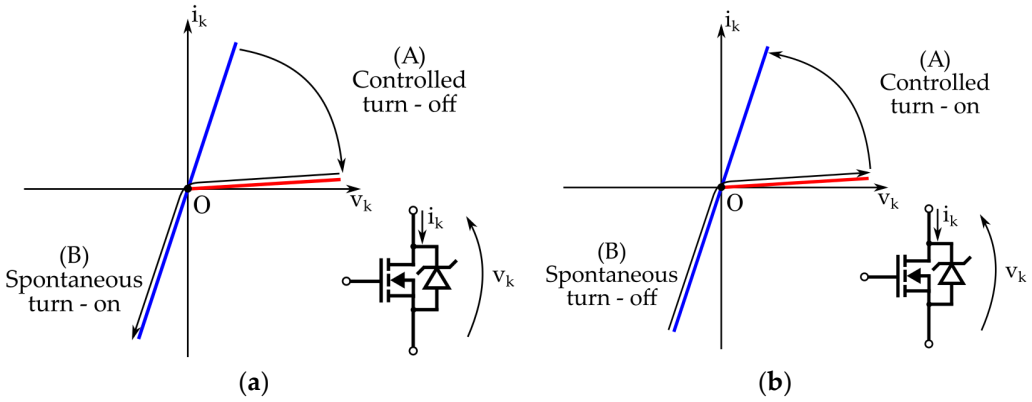

Figure 3. Semiconductor device operation: (**a**) zero-voltage switching (ZVS) and (**b**) zero-current switching (ZCS).

To select an efficient topology for PV applications, the first area of concern is the switching mode of the semiconductors. On the one hand, MV SiC metal–oxide–semiconductor field-effect transistors (MOSFETs) usually have a turn-on energy (E_{on}) that is two times higher than the turn-off energy (E_{off}) for a given condition. Therefore, the ZVS operation, in which devices have controlled turn-off and spontaneous turn-on capabilities, is preferred. On the other hand, the resonant circuit topology, which has a strong influence on the conduction losses of the semiconductors, needs to be selected. Qualitatively, the current in the semiconductors needs to be proportional to the load current to reach "high" efficiency [31]. In particular, when the input power of the converter increases, its conduction losses also need to increase. To achieve this, the parallel and series-parallel resonant DAB requires a switching frequency (f_{sw}) lower than the resonant frequency (f_o). Nonetheless, for these converters to operate in the ZVS mode, f_{sw} must be greater than f_o. Consequently, it is not possible to simultaneously obtain low switching and conduction losses. In contrast, the series resonant configuration offers high efficiency for PETs by providing both the ZVS mode and low conduction losses for switching devices. Thus, DAB converters using a series resonant circuit (C_r, L_r) (see Figure 4) are the most popular topology in high-power applications.

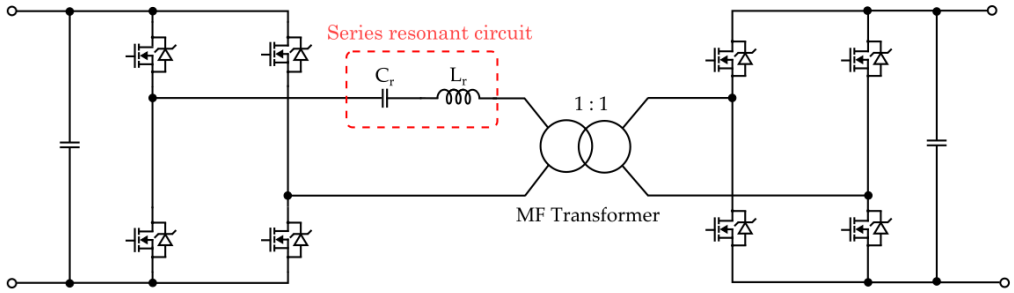

Figure 4. Series resonant dual active bridge (SR-DAB) converter.

The SR-DAB allows bidirectional power flow that is, however, not necessary in PV power plants. Therefore, the active rectifier is replaced by a diode bridge rectifier, which establishes a resonant single active bridge (R-SAB) converter, as shown in Figure 5. Furthermore, the R-SAB offers an output characteristic of the voltage source type [32].

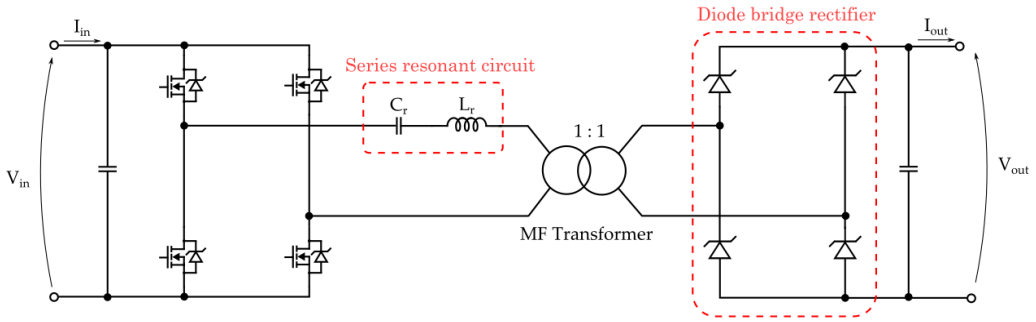

Figure 5. Resonant single active bridge (R-SAB) converter.

The R-SAB converter can operate in two modes:

- Continuous conduction mode (CCM): here, f_{sw} is higher than f_o ($f_{sw} > f_o$). The currents of the windings are continuous. The MOSFETs are turned off for currents proportional to the input power. The commutations of the rectifier's diodes depend completely on the AC currents of the transformer; therefore, power control is realized by either phase-shifted modulation of the inverter legs [33,34] or changing f_{sw} [32]. The latter method is preferred in this case since the phase-shifted modulation will cause current distortion in the circuit [35]. Moreover, this modulation technique can change the commutation mode of the switches. Thus, one of the inverter legs may operate in ZCS mode, which increases the switching losses.
- Discontinuous conduction mode (DCM): here, f_{sw} is less than f_o ($f_{sw} < f_o$), and the inverter legs are controlled in bipolar mode with a fixed duty cycle of 50%. The R-SAB converter is considered to be a passive device. The winding currents of the transformer reduce considerably at the end of each half of the switching period, and the MOSFETs are turned off at the magnetizing current of the transformer.

In the following subsections, these two operation modes are investigated to determine the most suitable mode for PV power generation.

3.1. R-SAB Converter with Intergrated Maximum Power Point Tracking (MPPT) Algorithm

To simplify the conversion energy system as much as possible, the isolated DC/DC converter needs to be able to realize the MPPT. Consequently, with the fixed output voltage (V_{out}), the R-SAB converter is directly connected to a PV array, and its input voltage (V_{in}) is controlled in such way that the PV array generates maximum power for a given condition. In CCM operation, the switching frequency (f_{sw}) can be determined as a function of the

input power (P_{in}). Referring to Figure 5, the output characteristic of the R-SAB converter is given as (1) [32]:

$$\left[\frac{V_{out}}{V_{in}}\sin\left(\frac{\pi}{2}\frac{f_o}{f_{sw}}\right)\right]^2+\left[\left(1+\frac{I_{out}}{V_{in}}\sqrt{\frac{L_r}{C_r}}\right)\cos\left(\frac{\pi}{2}\frac{f_o}{f_{sw}}\right)\right]^2=1 \quad (1)$$

where $f_o=\frac{1}{2\pi\sqrt{L_rC_r}}$—the resonant frequency of series resonant circuit.

I_{out}—the DC output current of the R-SAB converter.

Then, f_{sw} is determined by (2):

$$f_{sw}=\frac{\pi f_o}{2\arcsin\left\{\left[\frac{1-\left(1+\frac{P_{in}}{V_{in}V_{out}}\sqrt{\frac{L_r}{C_r}}\right)^2}{\left(\frac{V_{out}}{V_{in}}\right)^2-\left(1+\frac{P_{in}}{V_{in}V_{out}}\sqrt{\frac{L_r}{C_r}}\right)^2}\right]^{\frac{1}{2}}\right\}} \quad (2)$$

where $P_{in}=V_{in}.I_{in}=V_{out}.I_{out}$—the input power of the R-SAB converter.

I_{in}—the DC input current of the R-SAB converter.

Figure 6 is plotted based on Equations (1) and (2); it shows the variations in the switching frequency (f_{sw}) in the function of the input voltage and power (i.e., V_{in} and P_{in}) when the output voltage (V_{out}) is fixed at 1000 V. When P_{in} decreases, f_{sw} increases. Nonetheless, this frequency range is limited by transformer losses. Moreover, high switching frequencies induce high switching losses to power semiconductors, decreasing the efficiency of the converter. Consequently, this operation mode is not suitable for PV applications wherein the maximum power point (MPP) changes intermittently.

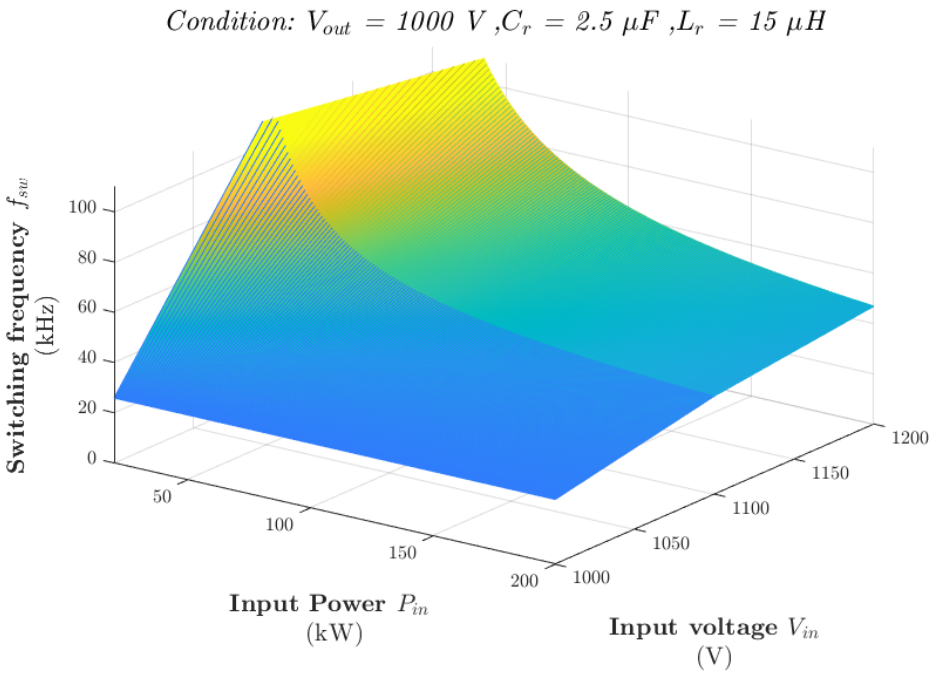

Figure 6. R-SAB converter operating in CCM with MPPT function based on switching frequency control: switching frequency (f_{sw}) versus input voltage and power (i.e., V_{in} and P_{in}).

3.2. PET with MPPT Boost Chopper

In this solution, the MPPT algorithm is performed using a boost chopper. Hence, in the topology presented in Figure 7, the galvanic isolation is realized by a PET that plays the role of a passive device. Thus, the PET can operate in DCM at a fixed frequency and quasi-constant voltage, which guarantees high-efficiency operations.

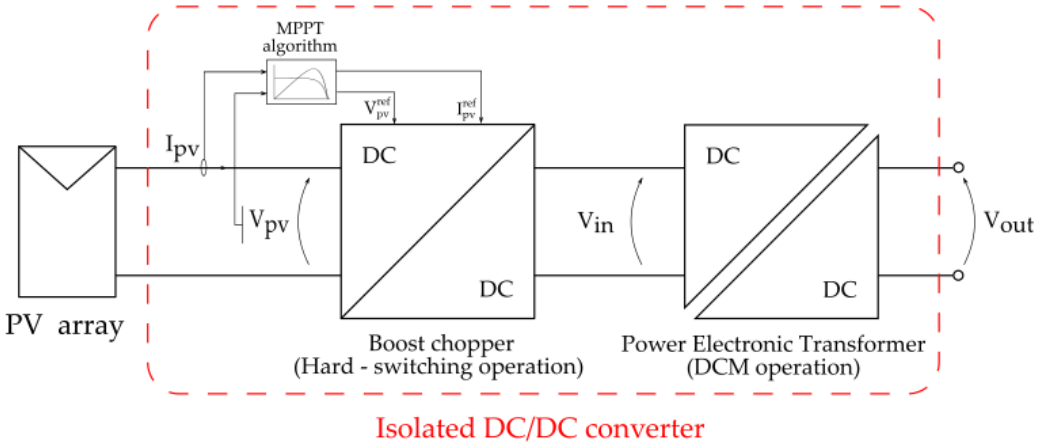

Figure 7. PET with MPPT boost chopper.

Thanks to the 3.3-kV SiC devices [9], open-circuit voltage (V_{oc}) of PV strings can be increased to 2 kV. The input voltage (V_{in}) of the PET is then fixed at 2 kV. The topology of the complete DC/DC converter using all the 3.3-kV SiC devices is shown in Figure 8a. Nevertheless, because of the long delivery time and high cost of 3.3-kV MOSFET modules, this paper presents two other solutions using 1.7-kV SiC MOSFET and 3.3-kV SiC diode modules. For the first case, a neutral point clamp (NPC) R-SAB converter is used, as shown in Figure 8b. In this case, the clamping diodes are used only for fixing the blocking voltage of each MOSFET at 1 kV; these diodes do not conduct or commutate, except during the dead time. Consequently, their power losses are negligible, and silicium diodes are sufficient. The main drawback of this topology comes from the capacitive midpoint of its input. The voltages across the capacitors are not automatically balanced; therefore, a control loop is required. Furthermore, in the NPC topology, the length of the commutation loop cannot be reduced, and high overvoltages can appear on MOSFETs during their commutation, which reduces the reliability of the converter. To overcome these problems, a new topology is proposed, as shown in Figure 8c. It is based on the input-series–output-parallel configuration (ISOP) of two R-SAB converters, in which MF transformers with a turn ratio of two are used. The ISOP arrangement allows natural voltage balance at the midpoint [36]. In addition, the length of the commutation loop in each chopper leg can be significantly reduced. Because of these advantages, a detailed study of this new topology of the isolated DC/DC converter is undertaken in this paper. The continuation of this subsection is divided into two parts. The first part will focus on the ISOP PET, that is, sizing and loss calculation. The second part will calculate the efficiency of the three-level MPPT boost chopper and then the complete isolated DC/DC converter.

3.2.1. Detailed Study on ISOP PET

This paper uses MF transformers (CEFEM Boige & Vignal, France). The characteristics of these transformers are given in Table 1. To optimize the ISOP PET layout, the total leakage inductance of the MF transformers is used as the resonant inductance (L_r). As shown in Figure 8c, resonant capacitors (i.e., C_p and C_s) are placed on both sides of the transformers to balance the overvoltages (due to resonant effect) across the two windings. In this case, the equivalent resonant capacitor (C_{req}) of the series resonant circuit is determined by (3):

$$\frac{1}{C_{req}} = \frac{1}{4C_s} + \frac{1}{C_p} \tag{3}$$

The resonant frequency (f_o) of the circuit is given by (4):

$$f_o = \frac{1}{2\pi\sqrt{L_r C_{req}}} \tag{4}$$

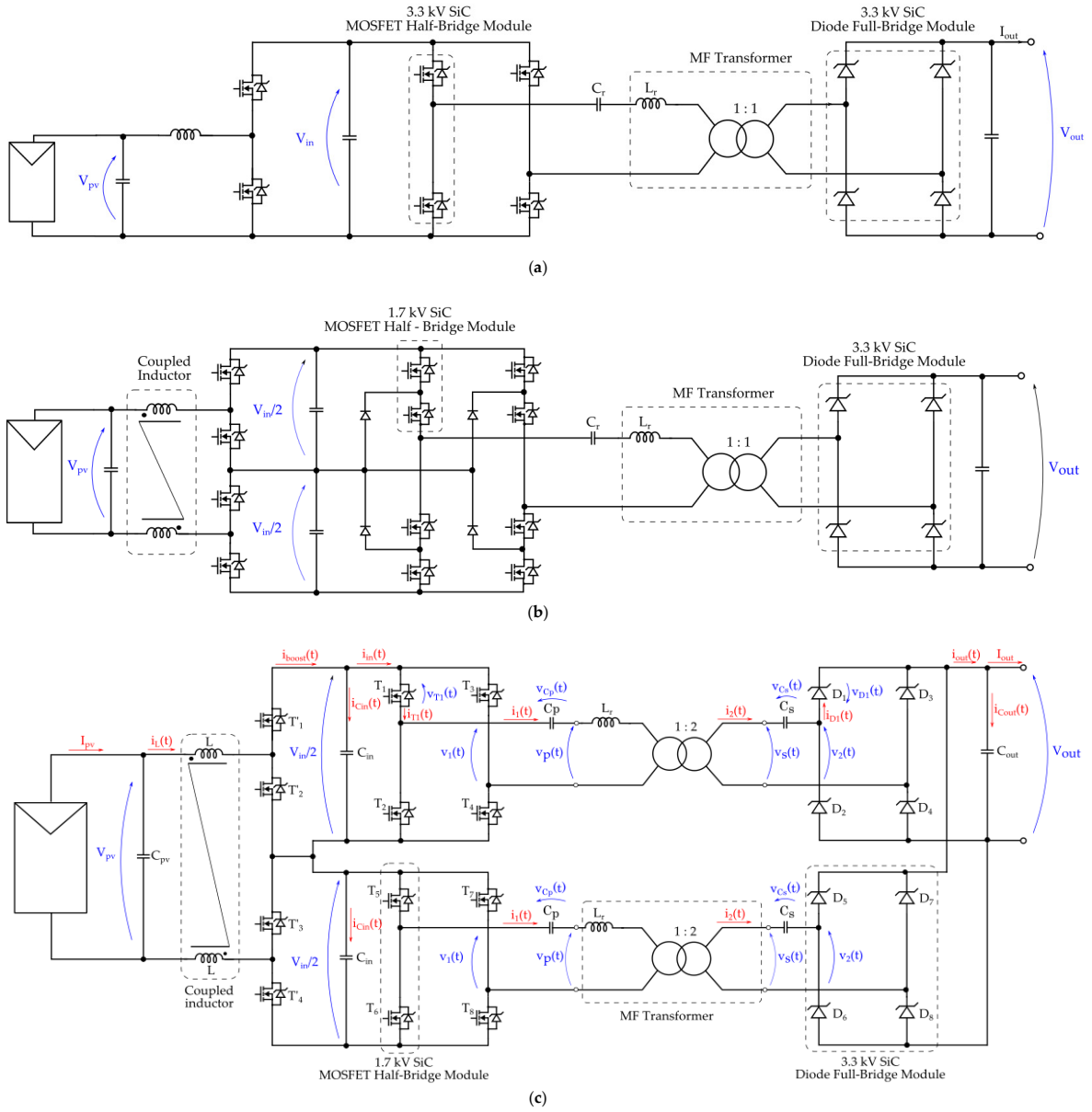

Figure 8. Isolated DC/DC converter for 2-kV PV strings using (**a**) all 3.3-kV SiC devices; (**b**) a 1.7-kV/3.3-kV SiC-based NPC PET; and (**c**) a 1.7-kV/3.3-kV SiC-based ISOP PET.

Table 1. Specifications of the MF transformers designed by CEFEM Boige & Vidal, France.

Nominal apparent power (S_n)	130 kVA
Turn ratio	1:2
Operation frequency	20–30 kHz
Nominal primary voltage	1000 V
Nominal secondary voltage	2000 V
Primary winding resistance (R_{cu1})	3 mΩ
Secondary winding resistance (R_{cu2})	16 mΩ
Core resistance referred to primary side (R_{fe})	5.5 kΩ @ 20 kHz 9.5 kΩ @ 30 kHz
Leakage inductance referred to primary side (L_{leak})	15 µH
Magnetizing inductance referred to primary side (L_m)	1 mH ± 30%
Magnetic material	Ferrite
Dimension	350 mm × 450 mm × 400 mm
Weight	30 kg

Knowing that f_{sw} is the switching frequency of the MOSFETs T_i ($i = \overline{1..8}$), the sizing of the resonant capacitors (i.e., C_p and C_s) is then based on the frequency ratio (f_{sw}/f_o). This frequency ratio has a significant impact on the current magnitude in the semiconductors. As V_{in} is fixed at 2 kV, the input current of the ISOP PET ($i_{in}(t)$) depends on the power provided by the PV array (P_{pv}), as well as the input power (P_{in}). Hence, its DC component (I_{in}) can be calculated by (5):

$$I_{in} = \frac{P_{pv}}{V_{in}} = \frac{P_{in}}{V_{in}} \tag{5}$$

The peak and average values of the current in the MOSFETs T_i ($i = \overline{1..8}$) are given by (6) and (7), respectively:

$$I_{Tpeak} = \frac{\pi}{2}\frac{f_o}{f_{sw}}I_{in} \tag{6}$$

$$I_{Tavg} = \frac{I_{in}}{2} \tag{7}$$

The relation between the current I_{in} and the root-mean-square (RMS) value of the current in these MOSFETs depends on the waveform of current $i_1(t)$. As has been established in [36], the RMS value of $i_1(t)$ can be calculated by (8):

$$I_{1rms} = \frac{\pi}{2\sqrt{2}}\sqrt{\frac{f_o}{f_{sw}}}I_{in} \tag{8}$$

Combining with (8), the RMS value of current in the MOSFETs T_i ($i = \overline{1..8}$) is determined by (9):

$$I_{Trms} = \sqrt{\frac{1}{T_{sw}}\int_0^{T_{sw}/2} i_1(t)dt} = \sqrt{\frac{1}{2}\cdot\left(\frac{1}{T_{sw}}\int_0^{T_{sw}} i_1(t)dt\right)} = \frac{1}{\sqrt{2}}I_{1rms} = \frac{\pi}{4}\sqrt{\frac{f_o}{f_{sw}}}I_{in} \tag{9}$$

where $T_{sw} = 1/f_{sw}$—the switching period of the MOSFETs.

Assuming that the voltage V_{in} and V_{out} are identical and considering the paralleling operation of the two diode bridge rectifiers, the peak, average, and RMS value of the current in the diodes D_j ($j = \overline{1..8}$) is given by (10), (11), and (12), respectively:

$$I_{Dpeak} = \frac{\pi}{4}\frac{f_o}{f_{sw}}I_{in} \tag{10}$$

$$I_{Davg} = \frac{I_{in}}{4} \tag{11}$$

$$I_{Drms} = \frac{\pi}{8}\sqrt{\frac{f_o}{f_{sw}}}I_{in} \tag{12}$$

The RMS value of the voltage across the resonant capacitors (i.e., C_p and C_s) is calculated by (13) and (14), respectively [36]:

$$V_{Cp} = \frac{I_{1rms}}{2\pi f_o C_p}\sqrt{2.\frac{f_{sw}}{f_o} - 1} \tag{13}$$

$$V_{Cs} = \frac{I_{2rms}}{2\pi f_o C_s}\sqrt{2.\frac{f_{sw}}{f_o} - 1} \tag{14}$$

where I_2—the RMS value of the current $i_2(t)$ in the resonant capacitor C_s.

From (9) and (12), it can be seen that, when f_{sw}/f_o is low, the switching devices need to conduct high RMS currents; consequently, they quickly reach their thermal limits. Moreover, from (13) and (14), low f_{sw}/f_o induces a high voltage across the resonant capacitors and, hence, overvoltages to the transformer windings because of the resonant effect. In contrast,

an f_{sw}/f_o close to unity does not allow ZVS operation for the SiC MOSFETs. Figure 9 illustrates the impact of different frequency ratios on the overvoltage at the transformer windings and on the conducting current of the semiconductors.

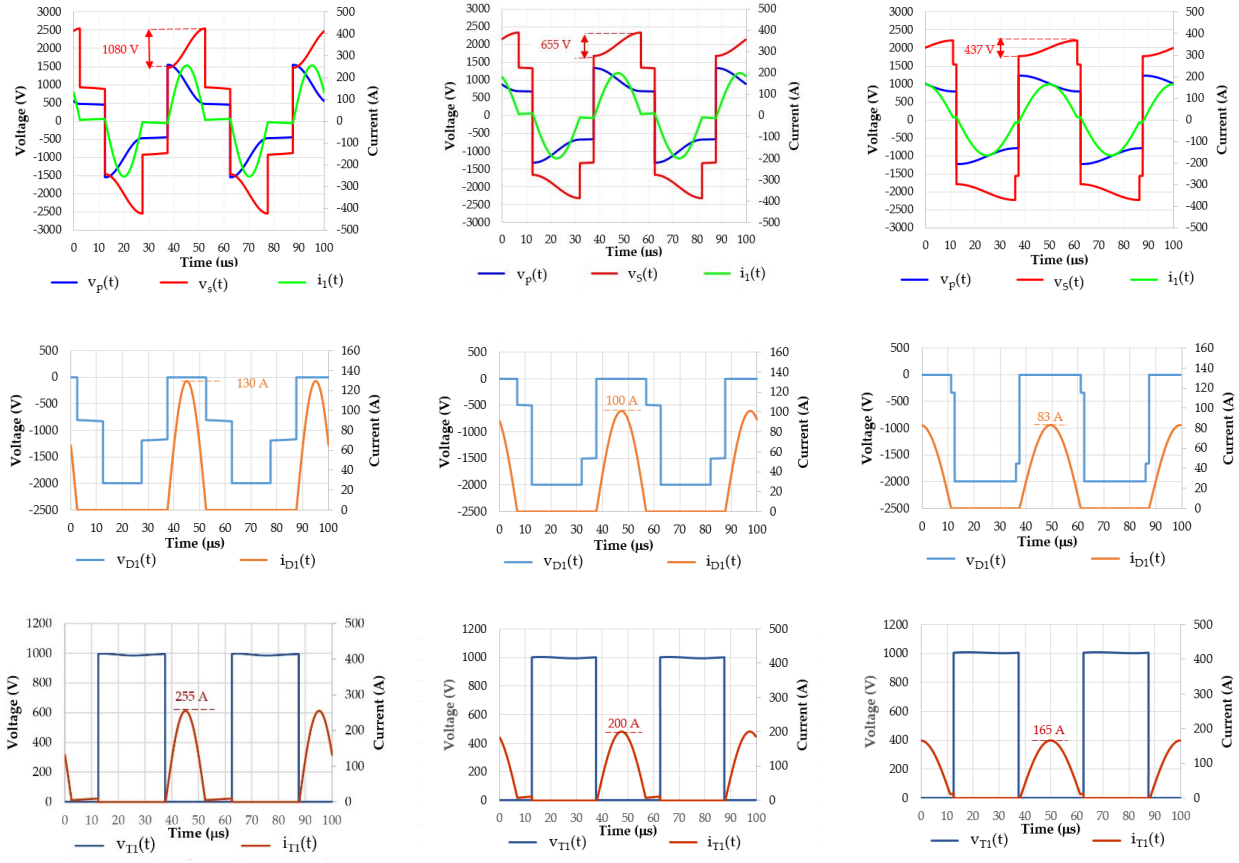

(**a**) (**b**) (c)

Figure 9. Isolated DC/DC converter of Figure 8c. Simulation waveforms with different frequency ratio (V_{in} = 2 kV, I_{in} = 100 A, f_{sw} = 20 kHz): (**a**) f_{sw}/f_o = 0.6; (**b**) f_{sw}/f_o = 0.8; (**c**) f_{sw}/f_o = 0.95.

The voltage applied to the transformer windings depends on the voltage across the resonant capacitors. Considering that windings would withstand the same overvoltage, from (13) and (14), the resonant capacitance ratio is given by (15):

$$\frac{C_p}{C_s} = \frac{I_{1rms}}{I_{2rms}} \cdot \frac{V_{Cs}}{V_{Cp}} = \frac{1}{2} \tag{15}$$

Combining (3), (4), and (15), the capacitance values for each transformer's side can be determined by (16):

$$\begin{cases} C_p = \frac{3}{2} C_{req} \\ C_s = \frac{3}{4} C_{req} \end{cases} \tag{16}$$

The sizing of the output capacitor (C_{out}) considers the maximum value of the voltage ripple across its terminals (ΔV_{Cout}). By using Fourier analysis, the current in the capacitor C_{out} is given by (17):

$$i_{Cout}(t) = \sum_{n=1}^{+\infty} \frac{2I_{in} \cos\left(\frac{f_{sw}}{f_o} n\pi\right)}{1 - \left(2\frac{f_{sw}}{f_o} n\right)^2} \cos\left(4n\pi f_{sw} t - \frac{f_{sw}}{f_o} n\pi\right) \tag{17}$$

From (17), the voltage ripple ΔV_{Cout} is mainly due to the first harmonic of the current $i_{Cout}(t)$. As a result, the maximum value of ΔV_{Cout} is determined by (18):

$$\mathrm{Max}\{\Delta V_{Cout}\} = \mathrm{Max}\left\{\frac{1}{C_{out}}\int i_{Cout}^{(1)}dt\right\} = \frac{\cos\left(\frac{f_{sw}}{f_o}\pi\right)}{2\pi f_{sw}C_{out}\left[1-\left(2\frac{f_{sw}}{f_o}\right)^2\right]}I_{in} \quad (18)$$

where $i_{Cout}^{(1)}$—the first harmonic of the current $i_{Cout}(t)$.

On the other hand, the voltage ripples of the input capacitors (C_{in}) depend on the harmonic currents induced by the boost chopper, as well as the ISOP PET. Hence, detailed calculations are demonstrated later in Section 3.2.2.

For switching devices, low-inductance 1.7-kV/353-A SiC MOSFET half-bridge modules and 3.3-kV/90-A full-bridge SiC Schottky diode modules from Microsemi Corporation are implemented. Their characteristics are given in Tables 2 and 3, respectively.

Table 2. Characteristics of the 1.7-kV/353-A half-bridge SiC MOSFET module from Microsemi.

		SiC MOSFET	**SiC Schottky Diode**
Electrical characteristics	Static characteristics (T_j = 175 °C)	R_{ds} = 11.1 mΩ	R_d = 7.5 mΩ
	Switching Characteristics [1] (V_{ds} = 0.9 kV, T_j = 175 °C)	$a_{on} = 2 \times 10^{-8}$, $b_{on} = 14 \times 10^{-5}$ $c_{on} = 1 \times 10^{-3}$	E_{on} = 0 J
		$a_{off} = 3 \times 10^{-8}$, $b_{off} = -0.15 \times 10^{-5}$ $c_{off} = 1.031.0 \times 10^{-3}$	E_{off} = 0 J
Thermal characteristics	Junction-to-Case Thermal resistance	$R_{th(j\text{-}c)T}$ = 0.09 K/W	$R_{th(j\text{-}c)D}$ = 0.1 K/W
	Maximum junction temperature	T_j^{max} = 175 °C	

[1] $E_{on/off} = a_{on/off}(V_{ds}, T_j).i_{on/off}^2 + b_{on/off}(V_{ds}, T_j).i_{on/off} + c_{on/off}(V_{ds}, T_j)$ Where $i_{on/off}$—turn-on/turn-off current of the MOSFETs.

Table 3. Characteristics of 3.3-kV/90-A full-bridge SiC diode module from Microsemi.

		SiC Schottky Diode
Electrical characteristics	Static characteristics (T_j = 175 °C)	R_d = 3.8 mΩ
	Switching characteristics	E_{sw} = 0 J
Thermal characteristics	Junction-to-Case Thermal resistance	$R_{th(j\text{-}c)D}$ = 0.1 K/W
	Maximum junction temperature	T_j^{max} = 175 °C

The efficiency calculation of the ISOP PET is now realized by simulations in the PLECS software [37]. The frequency ratio (f_{sw}/f_o) is then chosen to be 0.8 and the switching frequency (f_{sw}) is chosen as 20 kHz. For semiconductor loss calculation, PLECS software allows building of a loss model for switching devices based on look-up tables, which are derived from its static and switching curves in the manufacturer's datasheet. During on-state, PLECS software measures the device current and its junction temperature. By reading the look-up table, the on-state voltage is obtained, and the conduction loss is then calculated. For switching losses, PLECS software captures electrical quantities (v, i) of the semiconductor at the pre- and post-switching moments. Combining with the junction temperature, it uses these quantities to read the commutation energy corresponding to that defined in the look-up tables. The semiconductor losses are the sum of switching and

conduction losses. Then, combining with the thermal model, the junction temperature is updated. Iterative computations are performed to reach the steady-state operation point. For losses of the MF transformers, an electrical model with constant parameters, as shown in Figure 10, is built in PLECS based on the specifications presented in Table 1.

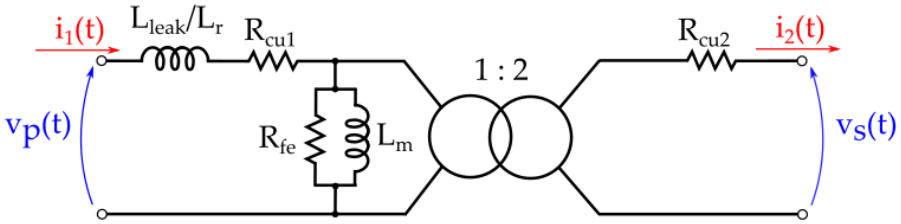

Figure 10. The electrical model of MF transformers used in PLECS software for their loss computation.

Throughout the simulations, the case temperature T_{case} of the power modules is supposed to be 85 °C. Then, the input power (P_{in}) is progressively increased. The nominal power of the ISOP PET is determined by the operation point where one of the semiconductors reaches its thermal limit (T_j^{max}= 175 °C) or the MF transformers reach their nominal power (S_n = 130 kVA). By considering the first harmonic of voltage waveform $v_1(t)$ (demonstrated by (19)), the apparent power ($S_{transfo}$) of each MF transformer for a given input power (P_{in}) can be estimated by (20). The ZVS operation was modeled by setting the turn-on energy of the MOSFETs T_i ($i = \overline{1..8}$) to zero in their loss model.

By Fourier analysis, the instantaneous value of $v_1(t)$ is rewritten by (19):

$$v_1(t) = \sum_{n=1}^{+\infty} \frac{2V_{in}}{n\pi} \sin\left(\frac{n\pi}{2}\right) \cos(2n\pi f_{sw} t) \tag{19}$$

The apparent power of the MF transformers is approximately estimated by (20):

$$S_{transfo} \approx V_{1rms}^{(1)} I_{1rms} = \frac{1}{2} V_{in} I_{in} \sqrt{\frac{f_o}{f_{sw}}} = \frac{1}{2} P_{in} \sqrt{\frac{f_o}{f_{sw}}} \tag{20}$$

where $V_{1rms}^{(1)}$—the RMS value of the first harmonic of the voltage $v_1(t)$.

The fixed parameters of the simulation are given in Table 4. The simulation results are shown in Figure 11.

Table 4. Simulation parameters for ISOP PET simulations.

DC input voltage (V_{in})	2000 V
DC output voltage (V_{out})	2000 V
Switching frequency (f_{sw})	20 kHz
Frequency Ratio (f_{sw}/f_o)	0.8
Resonant inductance (L_r)	15 µH
Resonant capacitance on primary side (C_p)	3.8 µF
Resonant capacitance on secondary side (C_s)	1.9 µF
Case temperature of MOSFET module (T_{case})	85 °C

It can be seen that the ISOP PET offers high efficiency (>99%) because of the ZVS and DCM operations. The 3.3-kV SiC diodes did not introduce any switching losses; there was only conduction loss in the rectifier part. On the inverter side, the switching losses of the MOSFETs remained constant because they were always turned off at the magnetizing current of the MF transformers, that is, relatively low. Their conduction losses increased with the input power. Note that, in these simulations, the turn-off energy of the MOSFETs is derived from the switching curves specified in their datasheets, which are obtained from double pulse tests (DPTs) for hard-switching applications. Consequently, the turn-off

loss in the simulation could be higher than the loss in practice. To obtain more accurate results, the characterizations of these MOSFETs under the ZVS test bench will be realized in the future [38]. Finally, the core loss of the transformers is constant and depends only on the magnetizing current. Their copper loss is proportional to the input power. Since semiconductor losses are low, they will operate below their thermal limits. Therefore, the power rating of the PET ISOP will be limited by the losses in the MF transformers.

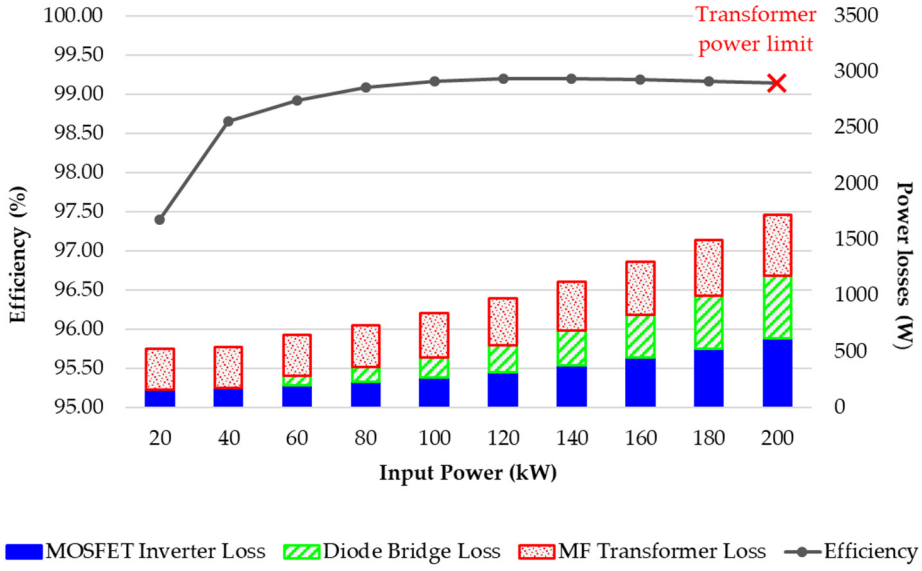

Figure 11. Simulation results: efficiency and power-loss repartition of ISOP PET.

3.2.2. Sizing and Evaluation of MPPT Three-Level Boost Chopper

In addition to adapting the voltage level for 1.7-kV SiC MOSFETs, another advantage of using the three-level boost chopper is that the interleaved control of the two switching cells (T'_1,T'_2) and (T'_3,T'_4) increases the apparent frequency of the its input current ($i_L(t)$). Moreover, the magnetic coupling of the two inductors limits their volume and increases the power density of the converter.

Knowing that the semiconductors T'_k ($k = \overline{1..4}$) switch at the frequency f_{boost}, the duty cycle (α_{boost}), which allows regulation of the PV array voltage (V_{pv}), is given by (21):

$$\alpha_{boost} = \frac{V_{pv}}{V_{in}} \tag{21}$$

The DC current I_{in} of the ISOP PET is determined by (22):

$$I_{in} = \alpha_{boost} I_{pv} \tag{22}$$

where I_{pv}—the DC current provided by the PV array when imposing the voltage V_{pv}.

The average and RMS values of the currents in the semiconductors T'_1 and T'_4 are calculated as (23) and (24), respectively:

$$I_{T'_1/T'_4 avg} = \alpha_{boost} I_{pv} \tag{23}$$

$$I_{T'_1/T'_4 rms} = I_{pv} \sqrt{\alpha_{boost}} \tag{24}$$

The average and RMS values of the current in the semiconductors T'_2 and T'_3 are calculated by (25) and (26), respectively:

$$I_{T'_2/T'_3 avg} = (1 - \alpha_{boost}) I_{pv} \tag{25}$$

$$I_{T'_2/T'_3rms} = I_{pv}\sqrt{1-\alpha_{boost}} \quad (26)$$

The sizing of input capacitors (C_{in}) is based on the analysis of current $i_{Cin}(t)$. As shown in Figure 8c, this current depends on the operation of boost chopper and the ISOP PET, which is expressed by (27):

$$i_{Cin}(t) = i_{boost}(t) - i_{in}(t) \quad (27)$$

where $i_{boost}(t)$—instantaneous value of the current outputted by the boost chopper.

By using Fourier analysis, the current $i_{boost}(t)$ can be calculated by (28):

$$i_{boost}(t) = I_{in} + \sum_{n=1}^{+\infty} \frac{2I_{pv}\sin(n\pi\alpha_{boost})}{n\pi}\cos(2n\pi f_{boost}t - \alpha_{boost}n\pi) \quad (28)$$

On the other hand, the current $i_{in}(t)$ is given by (29):

$$i_{in}(t) = I_{in} + \sum_{n=1}^{+\infty} \frac{2I_{in}\cos\left(\frac{f_{sw}}{f_o}n\pi\right)}{1-\left(2\frac{f_{sw}}{f_o}n\right)^2}\cos\left(4n\pi f_{sw}t - \frac{f_{sw}}{f_o}n\pi\right) \quad (29)$$

Combining (22), (27), (28), and (29), the voltage ripples of the capacitors C_{in} can be calculated by using (30):

$$\Delta v_{Cin}(t) = \frac{1}{C_{in}}\int i_{Cin}(t)dt = \sum_{n=1}^{+\infty}\frac{I_{pv}}{2n\pi}\left\{\frac{2\sin(n\pi\alpha_{boost})}{n\pi f_{boost}C_{in}}\sin(2n\pi f_{boost}t - \alpha_{boost}n\pi) - \frac{\alpha_{boost}\cos\left(\frac{f_{sw}}{f_o}n\pi\right)}{f_{sw}C_{in}\left[1-\left(2\frac{f_{sw}}{f_o}n\right)^2\right]}\sin\left(4n\pi f_{sw}t - \frac{f_{sw}}{f_o}n\pi\right)\right\} \quad (30)$$

The sizing of the capacitors (C_{in}) considers the maximum value of $\Delta v_{Cin}(t)$ calculated according to (30). Despite this analytical method being feasible, it is complex and time-consuming. The more direct way is to use PLECS software to determine numerically the value $\mathrm{Max}\{\Delta v_{Cin}(t)\}$.

Now, the efficiency computation of the boost chopper is realized. The voltage V_{in} of the chopper was fixed at the level of the ISOP PET in the previous part (i.e., 2 kV). The voltage V_{pv} is varied according to the MPP voltage range of a 2-kV PV string that is from 1 kV to 1.8 kV, corresponding to the PV cell temperature from 85 °C to −20 °C. The thermal model of the MOSFETs (i.e., T'_1, T'_2, T'_3, and T'_4) allows simulation of the hard-switching operation. The study also considers the losses of the coupled inductor (CEFEM Boige & Vidal, France). The characteristics of the inductor and the simulation parameters are presented in Tables 5 and 6, respectively.

Table 5. Coupled inductor designed by CEFEM Boige & Vidal, France.

Coupled inductor leakage inductance (L)	350 µH ± 10%
Rated DC current	180A
Current ripple	18 A @ 20 kHz
DC+AC winding resistance	3.7 mΩ
Core losses at 20 kHz	50 W
Magnetic material	Amorphous
Dimension	250 mm × 220 mm × 400 mm
Weight	40 kg

Table 6. Simulation parameters of the three-level boost chopper.

DC PV voltage (V_{pv})	1000–1800 V
DC output voltage (V_{in})	2000 V
Switching frequency (f_{boost})	10 kHz
Case temperature of power module (T_{case})	85 °C

The efficiency of the chopper is presented in Figure 12. Clearly, this converter offers high efficiency (>99.5%). In fact, the MOSFETs generate low losses, even if they operate in the hard-switching mode with a relatively high switching frequency. The additional losses are from the coupled inductor, in which the core losses are negligible.

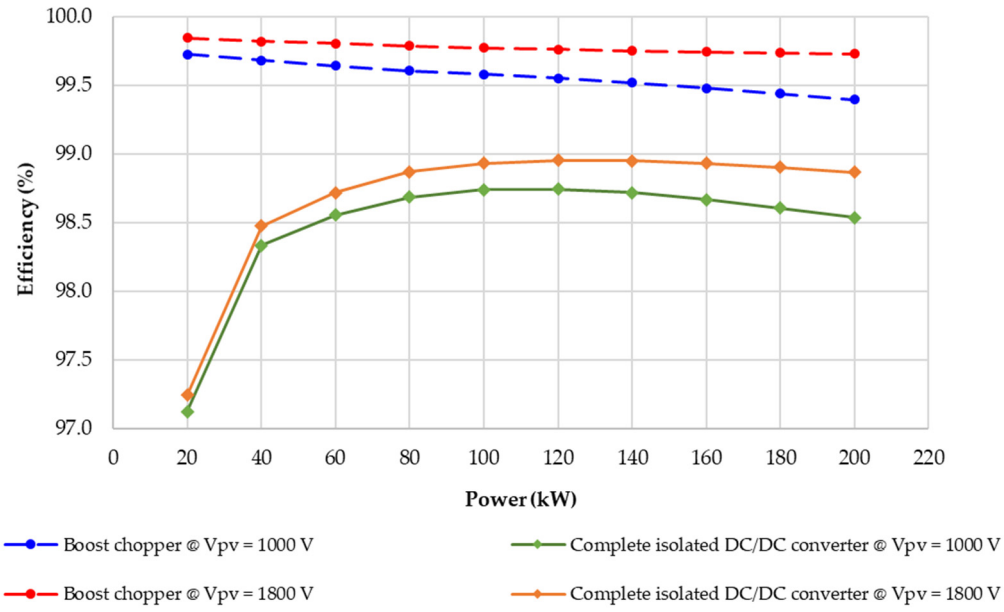

Figure 12. Simulation results: efficiency of the three-level boost chopper and complete isolated DC/DC converter for different voltage V_{pv}.

The overall efficiency of the complete isolated DC/DC converter is also plotted in the same figure by combining with the results of the previous part. The efficiency of the converter was greater than 98.5% for over 80% of the operating range. The maximum efficiency of 99% could be achieved when the PV array was in favorable ambient conditions with high solar irradiance and low temperature.

The proposed converter clearly offers an isolated device that has high efficiency and power density. These factors help eliminate bulky low-frequency transformers, which make the layout of the utility-scale PV power plants more optimal.

4. Conclusions and Future Work

This paper first presents the motivation for implementing isolated MV PV power plants. Then, a survey of the MV topologies is mentioned. In addition to those presented in the literature, new topologies with an intermediate MVDC collector that naturally cancels the current imbalance problem encountered on multiple MVAC collectors are introduced. In the second part, detailed analyses on the topologies of an isolated DC/DC converter were performed. By taking advantage of the fast-switching property of MV SiC switching devices, ISOP PET with a three-level boost chopper provides high efficiency (>98.5%) and high power density.

To validate the simulation results, a prototype based on ISOP PET with three-level boost choppers is under construction. The selected power modules will be characterized (switching and conduction losses) in order to determine more precisely the thermal model. Finally, the operation and efficiency of the isolated DC–DC converter will be evaluated and compared to simulation results.

Author Contributions: Methodology, P.L. and M.N.N.; software, M.N.N.; validation, P.L.; writing—original draft preparation, M.N.N.; writing—review and editing, M.N.N., P.L., J.M. and S.S. All authors have read and agreed to the published version of the manuscript.

Funding: This work was supported by the French National Program "Programme d'Investissements d'Avenir-INES.2S" under Grant ANR-10-IEED-0014-01.

Institutional Review Board Statement: Not applicable.

Informed Consent Statement: Not applicable.

Data Availability Statement: The data presented in this study are available on request from the corresponding author.

Conflicts of Interest: The authors declare no conflict of interest.

References

1. Jaeger-Waldau, A. *PV Status Report 2019*; EUR 29938 EN; Publications Office of the European Union: Luxembourg, 2019; ISBN 978-92-76-12608-9. [CrossRef]
2. Langner, A. *Photovoltaics Report*; Fraunhofer ISE: Freiburg, Germany, 2021.
3. Large-Scale Photovoltaic Power Plants-Top 50. Available online: https://www.pvresources.com/en/pvpowerplants/top50pv.php (accessed on 8 November 2021).
4. Alhuwaishel, F.; Allehyani, A.; Al-Obaidi, S.; Enjeti, P. A New Medium Voltage DC Collection Grid for Large Scale PV Power Plants with SiC Devices. In Proceedings of the 2018 IEEE 19th Workshop on Control and Modeling for Power Electronics (COMPEL), Padova, Italy, 25–28 June 2018; pp. 1–8. [CrossRef]
5. Rakhshani, E.; Rouzbehi, K.; Sánchez, A.; Tobar, A.C.; Pouresmaeil, E. Integration of Large Scale PV-Based Generation into Power Systems: A Survey. *Energies* **2019**, *12*, 1425. [CrossRef]
6. Bier, A.; Wiss, O.; Messaoudi, P. A 3 kV,18 kW Medium-Voltage PV Plant Demonstrator. Available online: https://docs.wixstatic.com/ugd/2c2db2_10c0956e790643b2829f75963fa5e187.pdf (accessed on 20 December 2021).
7. Platzer, W.; Boie, I.; Ragwitz, M.; Kost, C.; Thoma, J.; Vogel, A.; Fluri, T.; Pfeiffer, W.; Burmeister, F.; Tham, N.; et al. *Supergrid–Approach for the Integration of Renewable Energy in Europe and North Africa*, Fraunhofer ISE: Freiburg, Germany, 12 March 2016.
8. Scarpa, L.; Chicco, G.; Spertino, F.; Tumino, P.M.; Nunnari, M. Technical Solutions and Standards Upgrade for Photovoltaic Systems Operated Over 1500 Vdc. In Proceedings of the 2018 IEEE 4th International Forum on Research and Technology for Society and Industry (RTSI), Palermo, Italy, 10–13 September 2018; pp. 1–6.
9. Negishi, T.; Tsuda, R.; Ota, K.; Iura, S.; Yamaguchi, H. 3.3 kV All-SiC Power Module for Traction System Use. In Proceedings of the PCIM Europe 2017, International Exhibition and Conference for Power Electronics, Intelligent Motion, Renewable Energy and Energy Management, Nuremberg, Germany, 16–18 May 2017; pp. 1–6.
10. Murakami, T.; Sadamatsu, K.; Imaizumi, M.; Suekawa, E.; Hino, S. Comparative Study of Electrical Characteristics between Conventional and SBD-Embedded MOSFETs for next Generation 3.3kV SiC Modules. In Proceedings of the PCIM Europe digital days 2020, International Exhibition and Conference for Power Electronics, Intelligent Motion, Renewable Energy and Energy Management, Nuremberg, Germany, 7–8 July 2020; pp. 1–5.
11. Tafti, H.D.; Maswood, A.I.; Konstantinou, G.; Townsend, C.D.; Acuna, P.; Pou, J. Flexible Control of Photovoltaic Grid-Connected Cascaded H-Bridge Converters During Unbalanced Voltage Sags. *IEEE Trans. Ind. Electron.* **2018**, *65*, 6229–6238. [CrossRef]
12. Rivera, S.; Kouro, S.; Wu, B.; Leon, J.I.; Rodríguez, J.; Franquelo, L.G. Cascaded H-Bridge Multilevel Converter Multistring Topology for Large Scale Photovoltaic Systems. In Proceedings of the 2011 IEEE International Symposium on Industrial Electronics, Gdansk, Poland, 27–30 June 2011; pp. 1837–1844. [CrossRef]
13. Kouro, S.; Wu, B.; Moya, Á.; Villanueva, E.; Correa, P.; Rodríguez, J. Control of a Cascaded H-Bridge Multilevel Converter for Grid Connection of Photovoltaic Systems. In Proceedings of the 2009 35th Annual Conference of IEEE Industrial Electronics, Porto, Portugal, 3–5 November 2009; pp. 3976–3982. [CrossRef]
14. Zhang, X.; Wang, M.; Zhao, T.; Mao, W.; Hu, Y.; Cao, R. Topological Comparison and Analysis of Medium-Voltage and High-Power Direct-Linked PV Inverter. *CES Trans. Electr. Mach. Syst.* **2019**, *3*, 327–334. [CrossRef]
15. Bayat, H.; Yazdani, A. A Hybrid MMC-Based Photovoltaic and Battery Energy Storage System. *IEEE Power Energy Technol. Syst. J.* **2019**, *6*, 32–40. [CrossRef]
16. Ertasgin, G.; Whaley, D.M.; Ertugrul, N.; Soong, W.L. Analysis of DC Link Energy Storage for Single-Phase Grid-Connected PV Inverters. *Electronics* **2019**, *8*, 601. [CrossRef]
17. Islam, M.R.; Guo, Y.; Zhu, J. Multiple-Input Multiple-Output Medium Frequency-Link Based Medium Voltage Inverter for Direct Grid Connection of Photovoltaic Arrays. In Proceedings of the 2013 International Conference on Electrical Machines and Systems (ICEMS), Busan, Korea, 26–29 October 2013; pp. 202–207. [CrossRef]
18. Islam, M.R.; Guo, Y.; Zhu, J. A Multilevel Medium-Voltage Inverter for Step-Up-Transformer-Less Grid Connection of Photovoltaic Power Plants. *IEEE J. Photovolt.* **2014**, *4*, 881–889. [CrossRef]
19. Islam, R.; Mahfuz-Ur-Rahman, A.M.; Muttaqi, K.M.; Sutanto, D. State-of-the-Art of the Medium-Voltage Power Converter Technologies for Grid Integration of Solar Photovoltaic Power Plants. *IEEE Trans. Energy Convers.* **2019**, *34*, 372–384. [CrossRef]
20. Lesnicar, A.; Marquardt, R. An Innovative Modular Multilevel Converter Topology Suitable for a Wide Power Range. In Proceedings of the 2003 IEEE Bologna Power Tech Conference Proceedings, Bologna, Italy, 14 June 2003; Volume 3, p. 6. [CrossRef]

21. Ladoux, P.; Serbia, N.; Marino, P.; Rubino, L. Comparative Study of Variant Topologies for MMC. In *Automation and Motion 2014 International Symposium on Power Electronics, Electrical Drives*; IEEE: Ischia, Italy, 2014; pp. 659–664. [CrossRef]
22. M2C–It's Short for "Innovation". Available online: https://new.siemens.com/fr/fr/produits/automatisation-entrainements/variateurs/medium-voltage-converters/m2c-technology.html (accessed on 20 December 2021).
23. Sinamics Perfect Harmony GH150. Available online: https://new.siemens.com/global/en/products/drives/sinamics/medium-voltage-converters/sinamics-perfect-harmony-gh150.html (accessed on 20 December 2021).
24. Sinamics SH150. Available online: https://new.siemens.com/fr/fr/produits/automatisation-entrainements/variateurs/medium-voltage-converters/sinamics-sh150.html (accessed on 20 December 2021).
25. Lagier, T.; Dworakowski, P.; Buttay, C.; Ladoux, P.; Wilk, A.; Camail, P.; Anak Justin, E.C. Experimental Validation and Comparison of a SiC MOSFET Based 100 kW 1.2 kV 20 KHz Three-Phase Dual Active Bridge Converter Using Two Vector Groups. In Proceedings of the 2020 22nd European Conference on Power Electronics and Applications (EPE'20 ECCE Europe), Lyon, France, 7–11 September 2020; pp. 1–9.
26. Czyz, P.; Guillod, T.; Krismer, F.; Huber, J.; Kolar, J.W. Design and Experimental Analysis of 166 kW Medium-Voltage Medium-Frequency Air-Core Transformer for 1:1-DCX Applications. *IEEE J. Emerg. Sel. Top. Power Electron.* **2021**, *6*, 506. [CrossRef]
27. Mcmurray, W. Power Converter Circuits Having A High Frequency Link. *Heredity* **1970**, *23*, 3517300.
28. McMurray, W. The Thyristor Electronic Transformer: A Power Converter Using a High-Frequency Link. *IEEE Trans. Ind. Gen. Appl.* **1971**, *7*, 451–457. [CrossRef]
29. Perrin, R. La commutation douce: Le cas du convertisseur Flyback. *Symp. Genie Electr.* **2017**, *20*, 166. [CrossRef]
30. Fortes, G.; Ladoux, P.; Fabre, J.; Flumian, D. Characterization of a 300 kW Isolated DC-DC Converter Using 3.3 kV SiC-MOSFETs. In *PCIM Europe Digital Days 2021; International Exhibition and Conference for Power Electronics, Intelligent Motion, Renewable Energy and Energy Management*; Éditions TI. Saint Denis: Saint-Denis, France, 2021; pp. 1–8.
31. Erickson, R.; Maksimovic, D. *Fundamentals of Power Electronics*; Springer: Berlin/Heidelberg, Germany, 2001.
32. Foch, H.; Ladoux, P.; Piquet, H. Association de convertisseurs assurant une liaison énergétique. *Tech. L'ingénieur Convert. Électriques Appl.* **2010**, *24*, 556.
33. De Doncker, R.W.A.A.; Divan, D.M.; Kheraluwala, M.H. A Three-Phase Soft-Switched High-Power-Density DC/DC Converter for High-Power Applications. *IEEE Trans. Ind. Appl.* **1991**, *27*, 63–73. [CrossRef]
34. Xie, Y.; Ghaemi, R.; Sun, J.; Freudenberg, J.S. Implicit Model Predictive Control of a Full Bridge DC–DC Converter. *IEEE Trans. Power Electron.* **2009**, *24*, 2704–2713. [CrossRef]
35. Krismer, F. Modeling and Optimization of Bidirectional Dual Active Bridge DC-DC Converter Topologies. Ph.D. Thesis, ETH Zurich, Zürich, Switzerland, 2010. [CrossRef]
36. Fabre, J.; Ladoux, P.; Caron, H.; Verdicchio, A.; Blaquière, J.-M.; Flumian, D.; Sanchez, S. Characterization and Implementation of Resonant Isolated DC/DC Converters for Future MVdc Railway Electrification Systems. *IEEE Trans. Transp. Electrif.* **2021**, *7*, 854–869. [CrossRef]
37. PLECS | Plexim. Available online: https://www.plexim.com/products/plecs (accessed on 20 December 2021).
38. Fabre, J.; Blaquière, J.-M.; Verdicchio, A.; Ladoux, P.; Sanchez, S. Characterization in ZVS Mode of SiC MOSFET Modules for MVDC Applications. In Proceedings of the 2019 International Conference on Clean Electrical Power (ICCEP), Puglia, Italy, 2–4 July 2019; pp. 470–477. [CrossRef]